ARTICLE

Hydroxide promotes carbon dioxide electroreduction to ethanol on copper via tuning of adsorbed hydrogen

Mingchuan Luo[1,3], Ziyun Wang [1,3], Yuguang C. Li [1,3], Jun Li [1,2], Fengwang Li [1], Yanwei Lum [1], Dae-Hyun Nam [1], Bin Chen[1], Joshua Wicks [1], Aoni Xu[1], Taotao Zhuang[1], Wan Ru Leow[1], Xue Wang [1], Cao-Thang Dinh [1], Ying Wang [1], Yuhang Wang [1], David Sinton [2] & Edward H. Sargent [1*]

Producing liquid fuels such as ethanol from CO_2, H_2O, and renewable electricity offers a route to store sustainable energy. The search for efficient electrocatalysts for the CO_2 reduction reaction relies on tuning the adsorption strength of carbonaceous intermediates. Here, we report a complementary approach in which we utilize hydroxide and oxide doping of a catalyst surface to tune the adsorbed hydrogen on Cu. Density functional theory studies indicate that this doping accelerates water dissociation and changes the hydrogen adsorption energy on Cu. We synthesize and investigate a suite of metal-hydroxide-interface-doped-Cu catalysts, and find that the most efficient, $Ce(OH)_x$-doped-Cu, exhibits an ethanol Faradaic efficiency of 43% and a partial current density of 128 mA cm^{-2}. Mechanistic studies, wherein we combine investigation of hydrogen evolution performance with the results of operando Raman spectroscopy, show that adsorbed hydrogen hydrogenates surface *HCCOH, a key intermediate whose fate determines branching to ethanol versus ethylene.

[1] Department of Electrical and Computer Engineering, University of Toronto, Toronto, Ontario M5S 1A4, Canada. [2] Department of Mechanical and Industrial Engineering, University of Toronto, Toronto, Ontario M5S 3G8, Canada. [3]These authors contributed equally: Mingchuan Luo, Ziyun Wang, Yuguang C. Li. *email: ted.sargent@utoronto.ca

The electrochemical generation of C_{2+} fuels and chemicals from CO_2 and H_2O enables the storage of intermittent renewable energy[1–6]. Substantial progress has been made in producing gaseous ethylene from the CO_2 reduction reaction (CO_2RR), and the Faradaic efficiency (FE) now exceeds 70% at an overpotential of 0.55 V (ref. [7]).

By contrast, the electrochemical conversion of CO_2 to liquid ethanol — a promising renewable fuel with high energy density and compatibility with existing storage and transportation infrastructure — has seen more limited progress thus far. Indeed, today's best CO_2 electrocatalysts fail to provide majority ethanol production, instead preferring ethylene[8–11].

The optimization of intermediate binding energetics provides a framework in which to evaluate and design for desired electro-catalytic performance[12,13]. For CO_2RR specifically, the binding energy of CO (ΔE_{CO}) is an important descriptor that has enabled the prediction of a number of promising CO_2RR candidates[14]. Experimental studies have similarly followed the correlation between adsorbed CO (CO_{ad}) as a function of alloying/doping with elements, including Zn (ref. [15]), Ag (refs [16–18]), Au (ref. [19]), S (ref. [20]), B (ref. [21]), and N (ref. [22]), as well as with engineering of facets[23] and morphology[24–26].

In spite of these impressive efforts, the FE of CO_2-to-ethanol remains below 25% if one focuses on studies that achieve commercially-relevant current densities (>100 mA cm^{-2}). Even if one includes results down to 6 mA cm^{-2}, it has reached only 29% FE.

The scaling relationships among the carbonaceous inter-mediates[27] along the multi-step reduction pathway to ethanol mean that it is difficult — if only a single site, and thus one degree of freedom, is relied upon to engineer catalyst adsorption energie s— to optimize ΔE_{CO} simultaneously with the initial CO_2 adsorption; as well as to optimize the site for ensuing carbon–carbon coupling; and to optimize also the subsequent hydrogenation step. The formation of ethanol with high FE will rely on accessing experimental degrees of freedom that engineer these steps.

We reasoned that, since hydrogen (H_{ad}) co-exists with carbon-based intermediates during CO_2RR, controlling its presence could potentially offer a new handle to help break the scaling relations. There exist hints at this possibility in the prior literature, such as in the proposed ethylene pathway in which hot water hydro-genates adsorbed *HCCOH, the penultimate reaction inter-mediate for both ethanol and ethylene[28]. Experimentally, the direct involvement of water in producing ethanol from CO_2RR was clarified in a recent isotopic study[29].

We, therefore, pursued means to activate near-surface water molecules with the goal of boosting the production of ethanol.

Our thinking was that cleaving the Cu–C bond of adsorbed *HCCOH could thereby be promoted, favoring thereby the electroproduction of ethanol.

We begin with an investigation of how surface H_{ad} affects the selectivity of CO_2RR on Cu. To this end, we designed a catalytic system that allows us to construct both hydroxide- and oxide-doped Cu having tunable surface H_{ad} coverage. DFT studies reveal that this new catalyst facilitates water dissociation and favors H_{ad} formation. We then synthesize Pourbaix-stable hydroxide-doped and oxide-doped Cu catalysts and investigate them both ex situ and in situ. In all cases, we achieve a notable increase in the ratio of ethanol to ethylene production, documenting fully a doubling on the doped-Cu catalysts compared to Cu.

The best of these, Ce(OH)$_x$-doped-Cu, reaches a FE of 43% for ethanol at an operating current density of 300 mA cm^{-2}. Mechanistic studies indicate that surface H_{ad} favors the ethanol pathway over ethylene.

Results

DFT investigations of the effect of H_{ad}. Since OH$^-$ plays a beneficial role in promoting carbon–carbon coupling[7,30], CO_2RR electrocatalysis is carried out today in neutral or alkaline aqueous environment. In this environment, H_2O molecules serve as the proton source for CO_2RR.

Cleavage of the H–OH bond is needed to form H_{ad} on catalytic surface — the Volmer step in the hydrogen evolution reaction, HER. This accounts for the slower HER rate in alkaline and neutral media relative to that in acidic media[31]. Previous studies have demonstrated that the introduction of hydroxides or oxides increases H_{ad} coverage by accelerating the water dissociation step[32,33]. The approach tunes H_{ad} without the need to modify the bulk pH.

We thus reasoned that doping Cu with a stable hydroxide or oxide could enhance the surface H_{ad}; yet allow us to maintain the alkaline environment that favors carbon–carbon coupling. We carried out DFT calculations on Ce oxide- and Mn oxide-doped-Cu(111) (see the Methods section for details). Ce and Mn oxides were chosen due to their Pourbaix-stability under the reducing potentials used in CO_2RR[34]. We examined the water dissociation energy and the H adsorption energy (E_H) on both bare and doped-Cu(111). Figure 1 and Supplementary Fig. 1 show that water dissociation is more favorable on the oxide/hydroxide-doped-Cu surface (by 0.48 eV and 0.39 eV for Ce and Mn oxide, respectively) in comparison with that on the pure Cu. The adsorption of hydrogen is also stabilized on the oxide-doped-Cu surface. E_H is more favorable on Mn oxide/Cu than that of Ce oxide/Cu, which suggests that doping metal oxides on Cu
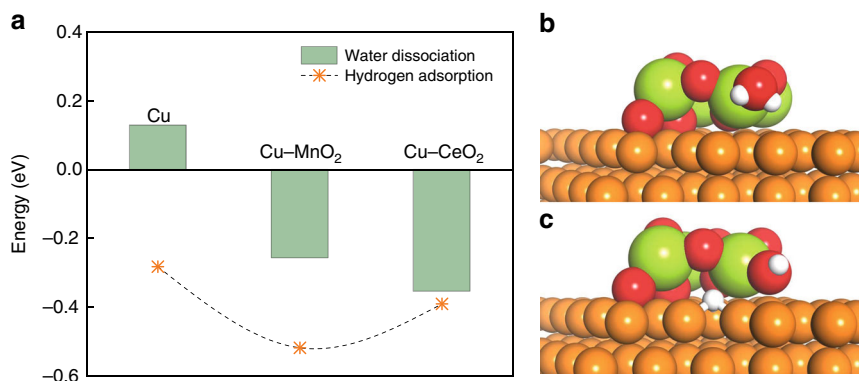
Fig. 1 Water activation on oxide-modified Cu surfaces. a Calculated water dissociation reaction energies and hydrogen adsorption energies on various surfaces. **b** Surface configurations of CeO$_2$/Cu with and **c** without adsorbed hydrogen.

provides the mean to control the extent of local H_{ad}. These findings suggested that building such hybrid catalysts could enable us to investigate and exploit H_{ad} in CO_2RR.

Catalyst synthesis and characterization. To synthesize the hybrid catalysts, we began with Cu-sputtered-polytetrafluoroethylene (Cu/PTFE) as the substrate[7], and we deposited either hydroxides or oxides via electrochemical or sputtering methods (Methods). The electrochemical deposition of metallic hydroxide was carried out in a neutral electrolyte containing the corresponding metallic nitrate as the precursor[35] (Supplementary Fig. 2). A cathodic current was first applied to the Cu/PTFE electrode to generate OH^- from nitrate reduction. The metallic hydroxide was then deposited onto the Cu surface via chemical reaction between the metallic cation and locally-generated OH^-. During the electrochemical deposition, the color of the Cu surface turned to brown.

To understand the nature of the doped hydroxides, we carried out characterization of the cerium hydroxide-doped-Cu/PTFE sample (denoted $Ce(OH)_x$/Cu/PTFE) using scanning electron microscopy (SEM), transmission electron microscopy (TEM) and scanning transmission electron microscopy (STEM), as well as X-ray diffraction (XRD) and X-ray photoelectron spectroscopy (XPS). Figure 2a shows the typical 3-dimensional networked structure after $Ce(OH)_x$ (Fig. 2a) electrochemically deposited into Cu/PTFE fibers. We propose that this structure facilitates CO_2 gas penetration to the triple-phase reaction region. STEM elemental mapping shows a homogeneous distribution of Cu and Ce throughout a single fiber (Fig. 2b). High-magnification SEM images of $Ce(OH)_x$/Cu/PTFE further reveal substantially uniformly-decorated nano-islands on the surface (Fig. 2c) with an average size of 18 nm and a typical range of 6–30 nm (Supplementary Fig. 3). High-resolution TEM reveals the interface between $Ce(OH)_x$ and Cu/PTFE (Fig. 2d). The

corresponding Fast Fourier Transform (FFT, the inset of Fig. 2d) pattern matches that of Cu_2O (111), indicating that the Cu/PTFE-based sample was partially oxidized. The oxidation of Cu is also seen in the XRD patterns of Cu/PTFE (Supplementary Fig. 4a), in which the diffraction peaks corresponding to both Cu and Cu_2O are observed.

The absence of observable lattice spacings in HRTEM, and a corresponding lack of crystalline peaks in XRD, suggest that the electrochemically-deposited $Ce(OH)_x$ exists in an amorphous structure, in agreement with the previous reports[35]. High-resolution XPS spectra for the Cu 2p region further show the co-existence of both metallic and oxidized states (Supplementary Fig. 4b). The Ce 3d spectra shows the co-existence of Ce^{4+} and Ce^{3+}, indicating that the deposition of cerium species (Supplementary Fig. 4c, d) was indeed achieved. The O 1s spectra confirm that the cerium species exist as hydroxide (Supplementary Fig. 4e).

Since the chemical states of metals are dependent on the applied potential[36], we carried out operando X-ray adsorption spectroscopy (XAS) to monitor the oxidation states of Cu and Ce during CO_2RR electrocatalysis by looking into the Cu K-edge and Ce L_3-edge, respectively. We found that — in agreement with the XPS results — Cu species were slightly oxidized before the reaction (Fig. 2e, Supplementary Fig. 5). However, once a negative potential had been applied during CO_2RR, only peaks corresponding to metallic Cu were observed (Supplementary Fig. 5). No change of Cu local structure (i.e., oxidation state, coordination number, and bond distance) was observed throughout CO_2RR process[37] (Supplementary Fig. 6 and Supplementary Table 1). Fig. 2f shows that, once a potential of -0.57 V vs. RHE was applied, the chemical state of Ce underwent an initial reduction. The ratio of Ce^{3+}/Ce^{4+} slightly increased from -0.57 V to -0.64 V vs. RHE, after which it remained unchanged upon further-increased reducing potentials. We conclude that an interface is
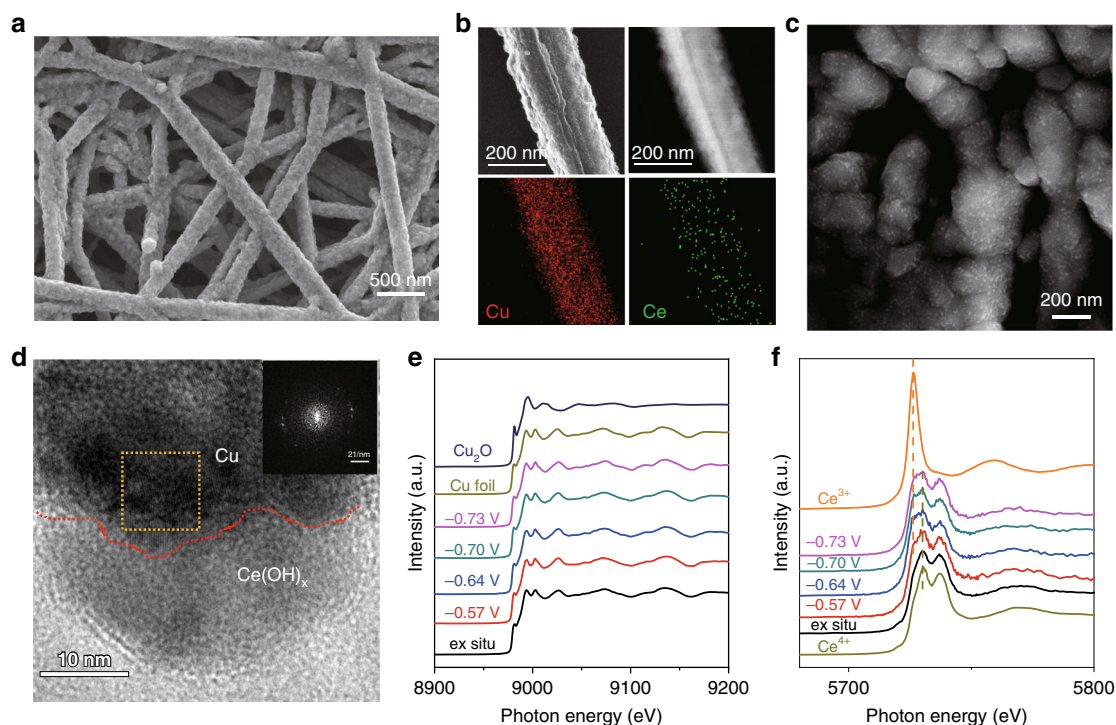
Fig. 2 Structural characterization of $Ce(OH)_x$ modified Cu catalysts. a Scanning electron microscope image, **b** STEM image and corresponding EDX mapping for Cu and Ce, **c** High-magnitude SEM image, **d** High-resolution transmission electron microscopy image of $Ce(OH)_x$/Cu/PTFE. The red dashed line draws attention to the interface, and the inset shows the FFT pattern corresponding to the yellow square. **e** Operando Cu K-edge and **f** operando Ce L_3-edge XAS of $Ce(OH)_x$/Cu/PTFE catalyst under a number of operating potentials in a flow cell.
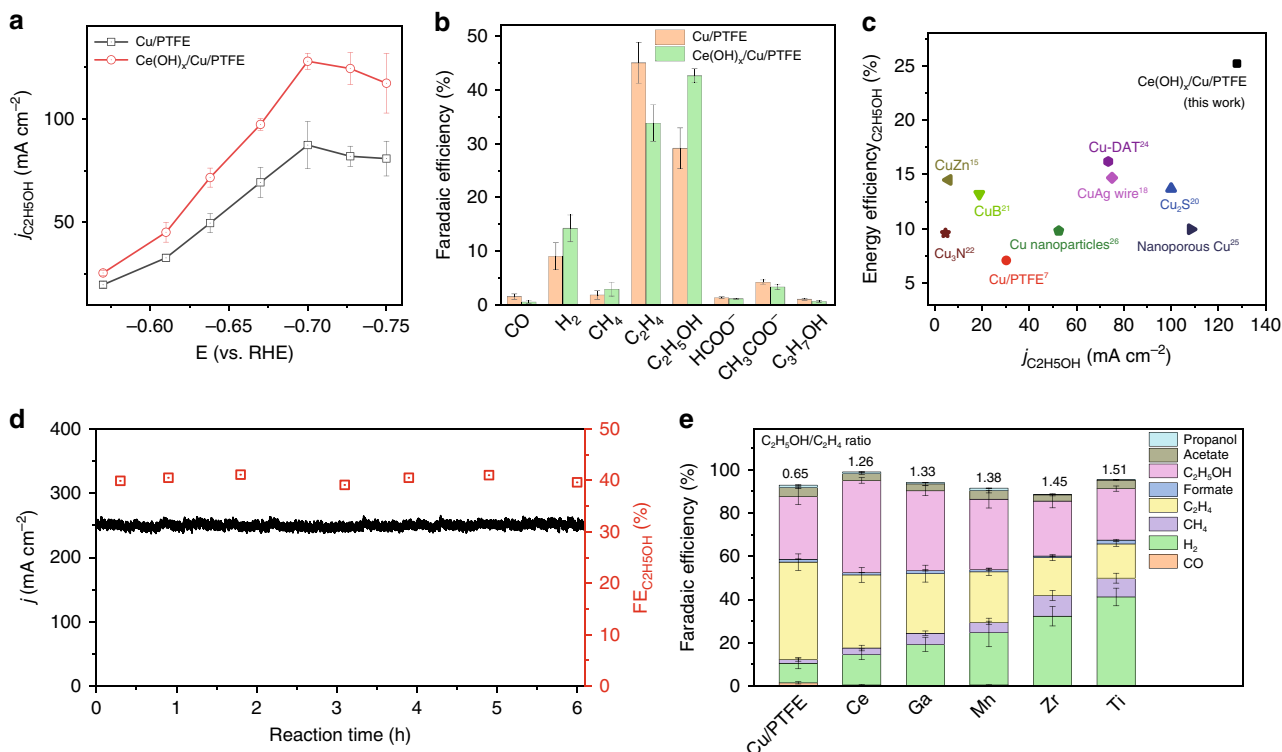
Fig. 3 Carbon dioxide electroreduction performance. a Partial ethanol current density of $Ce(OH)_x/Cu/PTFE$ and bare Cu/PTFE under various potentials. **b** Product distribution of $Ce(OH)_x/Cu/PTFE$ and bare Cu/PTFE at the −0.7 V versus RHE. **c** Energy efficiency as a function of partial current density on $Ce(OH)_x/Cu/PTFE$, in comparison with other reports with operational current density higher than 10 mA cm^{-2}. **d** i–t curve (left axis) of $Ce(OH)_x/Cu/PTFE$ catalyst along with corresponding Faradaic efficiency of ethanol (right axis). **e** Product distribution of various hydroxides/oxides modified Cu/PTFE electrode, along with corresponding C_2H_5OH/C_2H_4 ratio. The error bars represent the standard deviation from at least three independent tests.

provided between metallic Cu and oxidized Ce under the reducing conditions applied during CO_2RR electrocatalysis.

CO_2RR performance. Having established the structural properties of the $Ce(OH)_x/Cu/PTFE$ catalyst, we then assessed its CO_2RR performance. We used a flow cell set-up with 1 M KOH solution as the electrolyte and throughout included controls involving bare Cu/PTFE (Supplementary Fig. 7 and Supplementary Tables 2–5).

The FE for ethanol reached 43% when the $Ce(OH)_x/Cu/PTFE$ catalyst was employed — well above the value of 29% for the Cu control. The $Ce(OH)_x/Cu/PTFE$ catalyst also achieved an impressive partial current density, 128 mA cm^{-2} (Fig. 3a), for ethanol, compared to 87 mA cm^{-2} for the copper control. By comparing the product distributions at the optimal potentials, we found that $Ce(OH)_x$ doping had increased the FE toward H_2 by 5% compared to the Cu/PTFE baseline (Fig. 3b). This is consistent with DFT results that indicate that surface H_{ad} is enhanced via accelerated water dissociation and optimized hydrogen adsorption. The ethanol:ethylene ratio increased from 0.65 (Cu/PTFE) to 1.26 ($Ce(OH)_x/Cu/PTFE$), which is the highest among electrocatalysts that achieve a current density of >6 mA cm^{-2} (Supplementary Table 2). The energy efficiency as a function of partial current density for ethanol (Fig. 3c) reveals that the $Ce(OH)_x/Cu/PTFE$ achieved an energy efficiency of 25%. This is, by a factor of 1.6, the highest reported for systems operating above 10 mA cm^{-2} (Supplementary Table 6).

We also evaluated operating stability of the $Ce(OH)_x/Cu/PTFE$ catalyst. It provided stable operation over an initial 6 h at current density 250 mA cm^{-2} (Fig. 3d). TEM and SEM images of $Ce(OH)_x/Cu/PTFE$ electrode after reaction showed the preservation of the hydroxide/Cu interface, as well as of the well-dispersed Ce

$(OH)_x$ nano-islands on the sputtered Cu surface (Supplementary Fig. 8).

We used labeled $^{13}CO_2$ and confirmed that the ethanol was produced from CO_2. This test indicates that ethanol contamination is not a source of artefactual ethanol (Supplementary Fig. 9a). The small changes (within 3%) in electrochemically active surface area (ECSA) of the Cu/PTFE before and after the deposition of Ce $(OH)_x$ also excluded the influence of surface area differences on electrocatalytic performance (Supplementary Fig. 9b–d). Due to its electrical insulation, the PTFE substrate is not expected to affect ECSA measurements.

To investigate whether the materials design strategy herein offers a general way to tune CO_2RR selectivity, we further tested other stable hydroxide- and oxide-doped Cu catalysts including $Ga(OH)_3$, $Mn(OH)_3$, $Zr(OH)_4$ and TiO_2 (ref. [34]). A suite of microscopy and spectroscopy analysis confirmed they are structurally analogous with $Ce(OH)_x/Cu/PTFE$ (Supplementary Figs. 10–13). Similar electrocatalytic behaviors were observed in the doped samples: compared to Cu/PTFE controls, H_2 and CH_4 production increased, and C_2H_4 decreased (Fig. 3e). A positive correlation was observed between the FE ratio of ethanol/ethylene and the FE of H_2 (FE_{H2}), with $TiO_2/Cu/PTFE$ exhibiting the highest ethanol/ethylene ratio of 1.51. This agrees with the hypothesis that enhanced H_{ad} promotes ethanol over ethylene. The HER activities of the samples evaluated using the same flow cell system in Ar atmosphere showed the same trend as the FE_{H2} during CO_2RR; i.e., $TiO_2/Cu/PTFE > Zr(OH)_4/Cu/PTFE > Mn(OH)_3/Cu/PTFE > Ga(OH)_3/Cu/PTFE > Ce(OH)_x/Cu/PTFE$, further confirming the enhanced H_{ad} on Cu due to an accelerated Volmer step (Supplementary Fig. 14).

Mechanistic studies. We then sought further mechanistic insight into the selectivity of CO_2RR. Goddard and co-workers[28,38] have
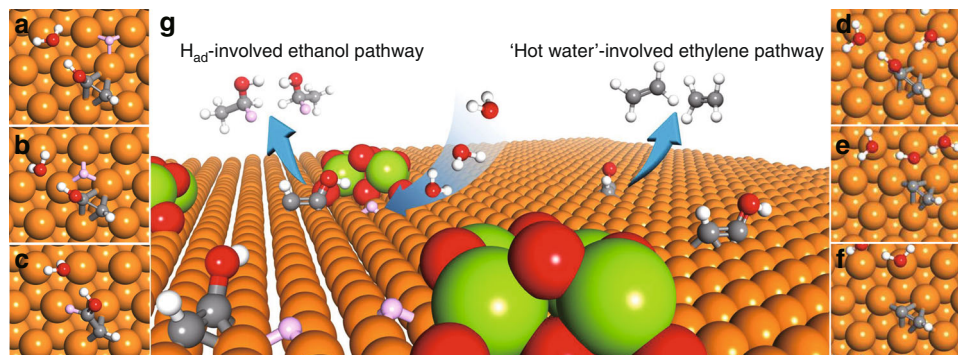
Fig. 4 Density functional theory calculations on the ethylene and ethanol pathways. Top views of geometries **a** initial state, **b** transition state, and **c** final state of key reaction towards ethanol, and **d** initial state, **e** transition state, and **f** final state of key reaction towards ethylene. Red, white, gray and orange balls stand for oxygen, hydrogen, carbon, and copper, respectively, while pink balls stand for H_{ad} on Cu.

previously shown that a key intermediate in the branching of ethylene vs. ethanol is *HCCOH (Fig. 4a, d). The ethylene pathway was proposed to be related to the removal of OH in *HCCOH (Fig. 4e) form *CCH (Fig. 4f); from which *CCH is then further hydrogenated, generating ethylene. In contradistinction, *HCCOH is hydrogenated into *HCCHOH (Fig. 4a–c) in the ethanol pathway.

As seen in Fig. 4d–f, surface water molecules are involved in the removal of OH: the hydroxyl group in *HCCOH is surrounded by five other water molecules with hydrogen bonds. In the transition state, the O–C bond between the hydroxyl group and *CCH dissociates with the help of surface water. In the final state, OH is stabilized by water and *CCH is formed. Thus, surface water plays an important role in the ethylene pathway. In the ethanol pathway, the H_{ad} attacks the *HCCOH (Fig. 4b), forming *HCCHOH, the key intermediate towards ethanol. H_{ad} is only involved in the branching reaction towards ethanol. When we enhance H_{ad} coverage, ethanol selectivity is enhanced (Fig. 4g).

To probe experimentally whether hydroxide modification also impacts the adsorption of carbonaceous intermediates on Cu, we carried out in situ Raman measurements and compared bare Cu/PTFE with $Ce(OH)_x$/Cu/PTFE across the potential region -0.24 to -0.73 V under CO_2RR (Supplementary Fig. 15). Due to their short life time, we are unable to provide direct experimental evidence for the *HCCOH intermediates; however, we found negligible influence of $Ce(OH)_x$ on adsorbed CO (CO_{ad}) — the Raman shift of frustrated rotation, and stretching, associated with Cu–CO, remained in the same position after $Ce(OH)_x$-modification of the Cu surface. Given the scaling relationship between CO_{ad} and other carbonaceous intermediates[14], we deduced that the electrocatalytic differences between bare Cu/PTFE and $Ce(OH)_x$/Cu/PTFE were unlikely to have originated from changes in the adsorption of carbonaceous species.

It is worth noting that the hydroxide deposition on Cu also promotes the CH_4 production from CO_2RR. Buonsanti and co-workers[39] recently reported the colloidal synthesis of a class of Cu/CeO_{2-x} heterodimers that showed a CO_2-to-CH_4 FE of 54% in $KHCO_3$ solution, exceeding the physically-mixed and individual controls. With the aid of DFT studies, they assigned the enhanced CH_4 production to the interface comprised of Cu, Ce, and O-vacancy sites that enabled breaking of the CHO*/CO* scaling relation. This mechanism investigated herein may contain analogies with how the hydroxide/Cu interface promotes CH_4 production through the C1 pathway.

Discussion

In summary, we reported an approach to higher-efficiency CO_2-to-ethanol conversion levering tuning of the adsorption of

hydrogen on Cu. The cerium hydroxide-doped copper catalyst provided a 43% FE at a total current density of 300 mA cm^{-2}. Mechanistic studies indicated that H_{ad} on Cu favors the ethanol over the ethylene pathway by attacking the Cu–C bond of the *HCCOH intermediate. The findings suggest further avenues to engineer hybrid catalysts that contribute multiple degrees of freedom to the design of multi-step CO_2 reduction reactions.

Methods

Electrode preparation. Cu/PTFE electrodes were prepared by sputtering a Cu layer of 300 nm in thickness onto a PTFE membrane (average pore size of 450 nm) using a Cu target (99.99%) at a rate of 1 Å s^{-1}.

Using the Cu/PTFE as the substrate, we electrochemically deposited various hydroxides in a three-electrode electrochemical cell. A potentiostat (Metrohm-Autolab, PGSTAT204) was used for the electrodeposition. The Cu/PTFE, a platinum foil and an Ag/AgCl electrode (saturated with KCl) were used as the working, counter and reference electrodes, respectively. The electrodeposition solution comprised 0.1 M KCl as the supporting electrolyte, and 0.025 M corresponding nitrate salts (cerium nitrate, 99.99%, Sigma-Aldrich; gallium nitrate, 99.9%, Sigma-Aldrich; zirconium oxynitrate, 99.99%, Sigma-Aldrich; manganese nitrate, 99.99%, Sigma-Aldrich) as the precursor. A current density of -0.5 mA cm^{-2} was held for a defined length of time (10, 20, 30, 40, and 50 min) to achieve varied surface coverage of hydroxides. Following the completion of the deposition, the working electrode was rinsed with DI water for at least three times and subsequently dried in N_2 atmosphere. Due to the instability of titanium nitrate, we deposited titanium oxides onto Cu/PTFE via a sequential sputtering of Cu followed by a layer of TiO_2 (5 nm).

Materials characterization. The morphology of the electrodes was characterized using scanning electron microscopy (SEM, Hitachi S-5200) with a 5-kV beam voltage. Transmission electron microscopy (TEM) and elemental mapping images were collected using a Hitachi HF-3300, at an acceleration voltage of 300 kV, equipped with a Bruker energy dispersive X-ray spectroscopy (EDX) detector. The acquisition time in the EDX studies was 3 min. Powder X-ray diffraction (XRD) patterns were recorded using a Bruker D8 using Cu-Kα radiation (λ = 0.15406 nm). X-ray photoelectron spectroscopy (XPS) was conducted on a PHI 5700 ESCA System using Al Kα X-ray radiation (1486.6 eV) for excitation. Operando X-ray absorption spectroscopy (XAS) investigations were carried out at the 9BM beamline of the Advanced Photon Source (APS) located in the Argonne National Laboratory (Lemont, IL). Detailed information regarding *operando* XAS tests in flow cells is available in a previous report[37]. Cu_2O, Cu foil, cerium oxide, and cerium oxalate hydrate were used as the reference samples. In situ Raman measurements were performed on a Renishaw inVia Raman Microscope in a modified flow cell and a water immersion objective (×63) with a 785 nm laser, using a 5 s integration and averaging 20 scans per region. In the above systems, platinum wire and an Ag/AgCl electrode were used as the counter and reference electrode, respectively.

Electrochemical measurements. Electrochemical studies were carried out using an electrochemical flow cell consisting of a gas chamber, a cathodic chamber, and an anodic chamber. The PTFE-based working electrode was fixed between the gas and cathodic chambers, with the catalysts layer side facing the cathodic chamber (geometric active surface area of 1 cm^2). An anion exchange membrane (Fumasep FAA-3-PK-130) was used to separate the anodic and cathodic chambers. All electrochemical tests were conducted on an Autolab PGSTAT204, with an Ag/AgCl electrode and Ni foam being the reference and counter electrodes, respectively. Potentials were converted to the reversible hydrogen electrode scale after iR

correction. Electrochemical impedance spectroscopy (EIS) in the frequency range of 10^5–10^{-1} Hz and an amplitude of 10 mV was used to determine the R value.

For performance studies, 1 M KOH was used as the electrolyte, and it was circulated through the cathodic and anodic chambers using peristaltic pumps at a rate of 10 mL min^{-1}. The flow rate of CO_2 gas through the gas chamber was controlled to be 50 sccm using a digital gas flow controller. Gas chromatography (PerkinElmer Clarus 600) with a flame ionization detector (FID) and a thermal conductivity detector (TCD) was used to analyze the gas products, collected from the end of the gas chamber. ^1H NMR spectroscopy (600 MHz, Agilent DD2 NMR Spectrometer) with water suppression was used to analyze the liquid products, using D_2O and DMSO as the lock solvent and internal reference, respectively. The hydrogen evolution reaction (HER) activities of various electrodes were evaluated in the same flow cell system, with the flow gas changed from CO_2 to Ar.

DFT calculations. All DFT calculations were carried out using the Vienna ab initio simulation program (VASP; https://vasp.at/)[40–43]. The projected augmented wave approach[44,45] was used to describe the electron-ion interactions with cutoff energy at 450 eV. The generalized gradient approximation with the Perdew, Burke and Ernzerhof exchange correlation functional was used[46]. For all the cerium related calculations, due to the strong correlations of the partially filled Ce 4f states, we employed the Hubbard parameter, U, to illustrate the on-site coulombic interaction[47]. A U–J value of 4.5 eV was chosen for Ce according to a previous study[48]. In order to illustrate the long-range dispersion interactions between the adsorbates and catalysts, we employed the D3 correction method by Grimme et al.[49]. Brillouin zone integration was accomplished using a $3 \times 3 \times 1$ Monkhorst-Pack k-point mesh. Four layers of Cu(111) surface was optimized, with the top 2 layers relaxed and bottom 2 layers fixed. Two molecular units of CeO_2 were introduced on to the Cu surface and optimized. To keep the model consistent, we replaced Ce atoms with Mn atoms and re-optimized the structure for the Mn oxide calculations. The water dissociation energy was calculated using $E_{dissociation} = E_{H_2O^*} - E_{H*+OH*}$, and the hydrogen adsorption energy was calculated using $E_{H_{ad}} = E_{H^*} + E_{slab} - 0.5E_{H_2}$, where * designates a surface adsorbed specie.

Data availability
The data that support the findings of this study are available from the corresponding author on reasonable request.

References
1. Gao, S. et al. Partially oxidized atomic cobalt layers for carbon dioxide electroreduction to liquid fuel. *Nature* **529**, 68–71 (2016).
2. Schreier, M. et al. Solar conversion of CO_2 to CO using earth-abundant electrocatalysts prepared by atomic layer modification of CuO. *Nat. Energy* **2**, 17087–17096 (2017).
3. Mariano, R. G., McKelvey, K., White, H. S. & Kanan, M. W. Selective increase in CO_2 electroreduction activity at grain-boundary surface terminations. *Science* **358**, 1187–1192 (2017).
4. Appel, A. M. et al. Frontiers, opportunities, and challenges in biochemical and chemical catalysis of CO_2 fixation. *Chem. Rev.* **113**, 6621–6658 (2013).
5. Liu, M. et al. Enhanced electrocatalytic CO_2 reduction via field-induced reagent concentration. *Nature* **537**, 382–386 (2016).
6. Mistry, H., Varela, A. S., Kühl, S., Strasser, P. & Cuenya, B. R. Nanostructured electrocatalysts with tunable activity and selectivity. *Nat. Rev. Mater.* **1**, 16009–16023 (2016).
7. Dinh, C. T. et al. CO_2 electroreduction to ethylene via hydroxide-mediated copper catalysis at an abrupt interface. *Science* **360**, 783–787 (2018).
8. Schouten, K. J., Calle-Vallejo, F. & Koper, M. T. A step closer to the electrochemical production of liquid fuels. *Angew. Chem. Int. Ed.* **53**, 10858–10860 (2014).
9. Verma, S., Kim, B., Jhong, H. R., Ma, S. & Kenis, P. J. A gross-margin model for defining technoeconomic benchmarks in the electroreduction of CO_2. *ChemSusChem* **9**, 1972–1979 (2016).
10. Bushuyev, O. S. et al. What should we make with CO_2 and how can we make It? *Joule* **2**, 825–832 (2018).
11. Spurgeon, J. M. & Kumar, B. A comparative technoeconomic analysis of pathways for commercial electrochemical CO_2 reduction to liquid products. *Energy Environ. Sci.* **11**, 1536–1551 (2018).
12. Seh, Z. W. et al. Combining theory and experiment in electrocatalysis: Insights into materials design. *Science* **355**, eaad4998 (2017).
13. Norskov, J. K., Bligaard, T., Rossmeisl, J. & Christensen, C. H. Towards the computational design of solid catalysts. *Nat. Chem.* **1**, 37–46 (2009).
14. Liu, X. et al. Understanding trends in electrochemical carbon dioxide reduction rates. *Nat. Commun.* **8**, 15438–15445 (2017).
15. Ren, D., Ang, B. S.-H. & Yeo, B. S. Tuning the selectivity of carbon dioxide electroreduction toward ethanol on oxide-derived Cu_xZn Catalysts. *ACS Catal.* **6**, 8239–8247 (2016).
16. Lee, S., Park, G. & Lee, J. Importance of Ag–Cu biphasic boundaries for selective electrochemical reduction of CO_2 to ethanol. *ACS Catal.* **7**, 8594–8604 (2017).
17. Clark, E. L., Hahn, C., Jaramillo, T. F. & Bell, A. T. Electrochemical CO_2 reduction over compressively strained CuAg surface alloys with enhanced multi-carbon oxygenate selectivity. *J. Am. Chem. Soc.* **139**, 15848–15857 (2017).
18. Hoang, T. T. H. et al. Nanoporous copper-silver alloys by additive-controlled electrodeposition for the selective electroreduction of CO_2 to ethylene and ethanol. *J. Am. Chem. Soc.* **140**, 5791–5797 (2018).
19. Morales-Guio, C. G. et al. Improved CO_2 reduction activity towards C^{2+} alcohols on a tandem gold on copper electrocatalyst. *Nat. Catal.* **1**, 764–771 (2018).
20. Zhuang, T.-T. et al. Steering post-C–C coupling selectivity enables high efficiency electroreduction of carbon dioxide to multi-carbon alcohols. *Nat. Catal.* **1**, 421–428 (2018).
21. Zhou, Y. et al. Dopant-induced electron localization drives CO_2 reduction to C_2 hydrocarbons. *Nat. Chem.* **10**, 974–980 (2018).
22. Liang, Z. Q. et al. Copper-on-nitride enhances the stable electrosynthesis of multi-carbon products from CO_2. *Nat. Commun.* **9**, 3828–3836 (2018).
23. Hahn, C. et al. Engineering Cu surfaces for the electrocatalytic conversion of CO_2: controlling selectivity toward oxygenates and hydrocarbons. *Proc. Natl Acad. Sci. USA* **114**, 5918–5923 (2017).
24. Hoang, T. T. H., Ma, S., Gold, J. I., Kenis, P. J. A. & Gewirth, A. A. Nanoporous copper films by additive-controlled electrodeposition: CO_2 Reduction catalysis. *ACS Catal.* **7**, 3313–3321 (2017).
25. Lv, J. J. et al. A highly porous copper electrocatalyst for carbon dioxide reduction. *Adv. Mater.* **30**, 1803111–1803119 (2018).
26. Ma, S. et al. One-step electrosynthesis of ethylene and ethanol from CO_2 in an alkaline electrolyzer. *J. Power Sources* **301**, 219–228 (2016).
27. Li, Y. & Sun, Q. Recent advances in breaking scaling relations for effective electrochemical conversion of CO_2. *Adv. Energy Mater.* **6**, 1600463–1600482 (2016).
28. Xiao, H., Cheng, T. & Goddard, W. A. III. Atomistic mechanisms underlying selectivities in C(1) and C(2) products from electrochemical reduction of CO on Cu(111). *J. Am. Chem. Soc.* **139**, 130–136 (2017).
29. Lum, Y., Cheng, T., Goddard, W. A. & Ager, J. W. Electrochemical CO reduction builds solvent water into oxygenate products. *J. Am. Chem. Soc.* **140**, 9337–9340 (2018).
30. Liu, X. et al. pH effects on the electrochemical reduction of $CO_{(2)}$ towards C_2 products on stepped copper. *Nat. Commun.* **10**, 32–42 (2019).
31. Subbaraman, R. et al. Enhancing hydrogen evolution activity in water splitting by tailoring Li^+-$Ni(OH)_2$-Pt interfaces. *Science* **334**, 1256–1260 (2011).
32. Dinh, C.-T. et al. Multi-site electrocatalysts for hydrogen evolution in neutral media by destabilization of water molecules. *Nat. Energy* **4**, 107–114 (2018).
33. Subbaraman, R. et al. Trends in activity for the water electrolyser reactions on 3d M(Ni,Co,Fe,Mn) hydr(oxy)oxide catalysts. *Nat. Mater.* **11**, 550–557 (2012).
34. Pourbaix, M. *Atlas of Electrochemical Equilibria in Aqueous Solutions* 2nd edn (National Association of Corrosion Engineers, 1974).
35. Ng, J. W. D. et al. Gold-supported cerium-doped NiO_x catalysts for water oxidation. *Nat. Energy* **1**, 16053–16061 (2016).
36. De Luna, P. et al. Catalyst electro-redeposition controls morphology and oxidation state for selective carbon dioxide reduction. *Nat. Catal.* **1**, 103–110 (2018).
37. Li, J. et al. Copper adparticle enabled selective electrosynthesis of n-propanol. *Nat. Commun.* **9**, 4614–4623 (2018).
38. Cheng, T., Xiao, H. & Goddard, W. A. Full atomistic reaction mechanism with kinetics for CO reduction on Cu(100) from ab initio molecular dynamics free-energy calculations at 298 K. *Proc. Natl Acad. Sci. USA* **114**, 1795–1800 (2017).
39. Varandili, S. B. et al. Synthesis of Cu/CeO_{2-x} nanocrystalline heterodimers with interfacial active sites to promote CO_2 electroreduction. *ACS Catal.* **9**, 5035–5046 (2019).
40. Kresse, G. & Furthmüller, J. Efficient iterative schemes for ab initio total-energy calculations using a plane-wave basis set. *Phys. Rev. B* **54**, 11169–11186 (1996).
41. Kresse, G. & Furthmüller, J. Efficiency of ab-initio total energy calculations for metals and semiconductors using a plane-wave basis set. *Comput. Mater. Sci.* **6**, 15–50 (1996).
42. Kresse, G. & Hafner, J. Ab initio molecular dynamics for liquid metals. *Phys. Rev. B* **47**, 558–561 (1993).
43. Kresse, G. & Hafner, J. Ab initio molecular-dynamics simulation of the liquid-metal–amorphous-semiconductor transition in germanium. *Phys. Rev. B* **49**, 14251–14269 (1994).
44. Blöchl, P. E. Projector augmented-wave method. *Phys. Rev. B* **50**, 17953–17979 (1994).

45. Kresse, G. & Joubert, D. From ultrasoft pseudopotentials to the projector augmented-wave method. *Phys. Rev. B* **59**, 1758–1775 (1999).
46. Perdew, J. P., Burke, K. & Ernzerhof, M. Generalized gradient approximation made simple. *Phys. Rev. Lett.* **77**, 3865–3868 (1996).
47. Dudarev, S. L., Botton, G. A., Savrasov, S. Y., Humphreys, C. J. & Sutton, A. P. Electron-energy-loss spectra and the structural stability of nickel oxide: An LSDA+U study. *Phys. Rev. B* **57**, 1505–1509 (1998).
48. Lustemberg, P. G. et al. Room-temperature activation of methane and dry reforming with CO_2 on Ni-CeO$_2$(111) surfaces: effect of Ce^{3+} sites and metal–support interactions on C–H bond cleavage. *ACS Catal.* **12**, 8184–8191 (2016).
49. Grimme, S., Antony, J., Ehrlich, S. & Krieg, H. A consistent and accurate ab initio parametrization of density functional dispersion correction (DFT-D) for the 94 elements H-Pu. *J. Chem. Phys.* **132**, 154104 (2010).

Acknowledgements

Author contributions
E.H.S. supervised the project. M.L. designed and carried out the experiments. Y.C.L. and Z.W. designed and carried out the DFT calculations. J.W., A.X., T.Z., and D.H.N. performed the XPS and XRD measurements. J.L., D.H.N., and Y.L. performed and analyzed the in situ XAS measurements. M.L. and F.L. performed and analyzed the Raman measurements. B.C. collected the STEM images and did the EDX mapping. W.L., Y.W., and X.W., collected the SEM images and did the EDX analysis. Y.H.W. prepared sputtered metal electrodes. C.T.D., D.S., and E.H.S. edited the paper. All authors discussed the results. M.L., Y.C.L., and Z.W. wrote the paper.

Competing interests
The authors declare no competing interests.

Additional information
Supplementary information is available for this paper at https://doi.org/10.1038/s41467-019-13833-8.

Correspondence and requests for materials should be addressed to E.H.S.

Peer review information *Nature Communications* thanks William Goddard and other, anonymous, reviewers for their contributions to the peer review of this work. Peer review reports are available.

Reprints and permission information is available at http://www.nature.com/reprints

Publisher's note Springer Nature remains neutral with regard to jurisdictional claims in published maps and institutional affiliations.